Configurable spatiotemporal properties in a photon-pair source based on spontaneous four-wave mixing with multiple transverse modes

Daniel Cruz-Delgado,[1] Jorge Monroy-Ruz,[1] Angela M. Barragan,[1] Erasto Ortiz-Ricardo,[1] Hector Cruz-Ramirez,[1] Roberto Ramirez-Alarcon,[1] Karina Garay-Palmett,[2] and Alfred B. U'Ren[1,*]

[1]*Instituto de Ciencias Nucleares, Universidad Nacional Autónoma de México, apdo. postal 70-543, 04510 D.F., Mexico*

[2]*Departamento de Óptica, Centro de Investigación Científica y de Educación Superior de Ensenada, Apartado Postal 360 Ensenada, BC 22860, Mexico*

**Corresponding author: alfred.uren@nucleares.unam.mx*

Received March 31, 2014; revised May 5, 2014; accepted May 10, 2014; posted May 13, 2014 (Doc. ID 209105); published June 10, 2014

We present an experimental and theoretical study of photon pairs generated by spontaneous four-wave mixing (SFWM), based on birefringent phasematching, in a fiber that supports more than one transverse mode. We present SFWM spectra, obtained through single-channel and coincidence photon counting, which exhibit multiple peaks shown here to be the result of multiple SFWM processes associated with different combinations of transverse modes for the pump, signal, and idler waves.

OCIS codes: (270.0270) Quantum optics; (190.4410) Nonlinear optics, parametric processes.
http://dx.doi.org/10.1364/OL.39.003583

The generation of photon pairs with configurable spatiotemporal entanglement is currently an important goal of quantum optics [1]. In this context, transverse optical confinement is a valuable resource for source design based on spontaneous parametric downconversion (SPDC) and spontaneous four-wave mixing (SFWM). In this work, we rely on the latter process, in a medium with a third-order nonlinearity, for which pairs of pump photons are annihilated, which leads to the emission of signal and idler photon pairs.

While the use of multiple transverse waveguide modes has been studied for SPDC [2–5] and for spontaneously-seeded *stimulated* FWM [6], it remains unexplored for SFWM. Without confinement, as in a bulk-crystal SPDC, the emission angles are strongly correlated to the frequencies, which leads to complex spatiotemporal entanglement characteristics [7]. In the opposite limit, where generation occurs in a single transverse mode, spectral properties become decoupled from the waveguide-determined spatial structure of the photon pairs, which also results in spatial factorability. This Letter studies the intermediate regimes where the controlled presence of more than one transverse mode becomes an effective tool to tailor the spatiotemporal photon-pair entanglement.

Our work looks at SFWM in a fiber that supports more than one transverse mode for the pump and the signal/idler waves. Under these circumstances, it is possible to obtain the coherent addition of distinct SFWM processes corresponding to different combinations of transverse modes for the four waves involved. Interestingly, phase matching couples the emission frequencies to specific combinations of transverse modes so that appropriate spectral filtering may be used to post-select specific SFWM processes. The experimenter can then ensure spatial factorability, if a single process is post-selected, or can permit a controlled type and degree of spatiotemporal entanglement, if several processes are post-selected.

Here we experimentally and theoretically studied cross-polarized SFWM in a birefringent fiber [8–12], where we concentrated on the as-yet-unexplored effects of the presence of more than one transverse mode. We measured the spectral structure of the photon pairs by single-channel and coincidence photon counting. A careful comparison with simulations allowed us, for what we believe is the first time, to identify the distinct spectral peaks observed with particular combinations of transverse modes for the pump and signal/idler photons. We thus determined the SFWM photon-pair spatiotemporal structure. In contrast to related guided-wave SPDC results [2], which resort to numerical mode analysis, the transverse mode structure in our fibers can be closely approximated by well-known linearly polarized (*LP*) modes. Also, our spectral emission peaks do not overlap one another (see the one exception below) ensuring mode orthogonality and the ability to fully separate the processes by frequency.

The two-photon component of the SFWM state, which exhibits entanglement in the transverse mode and spectral degrees of freedom, may be written as:

$$|\Psi\rangle = \sum_m \sum_n \int \mathrm{d}\omega_s \int \mathrm{d}\omega_i G_{mn}(\omega_s,\omega_i)|\omega_s;m\rangle|\omega_i;n\rangle, \quad (1)$$

where $|\omega;m\rangle_\mu \equiv a^\dagger(\omega;m)|0\rangle_\mu$ is a single-photon Fock state with frequency ω, transverse mode m, and for wave μ (with $\mu = s, i$ for signal and idler). $G_{mn}(\omega_s,\omega_i)$ is the joint amplitude involving a signal photon in transverse mode m and an idler photon in mode n. It is written as:

$$G_{mn}(\omega_s,\omega_i) = \sum_p \sum_q W_p W_q \gamma_{pqmn} \int \mathrm{d}\omega \alpha(\omega) \times \alpha(\omega_s+\omega_i-\omega)\mathrm{sinc}\left[\frac{L}{2}\Delta k_{pqmn}\right], \quad (2)$$

with sums over the pump transverse modes [13], and where W_p is the fraction of the pump power coupled into the fiber, in mode p; the sum over all W_s is unity. $\alpha(\omega)$ is the pump spectral amplitude, L is the fiber length, and $\Delta k_{pqmn} = k_p(\omega) + k_q(\omega_s+\omega_i-\omega) - k_m(\omega_s) - k_n(\omega_i)$,

with $k_\mu(\omega)$ the wavenumber for mode μ; note that a nonlinear term proportional to pump power has been disregarded. γ_{pqmn} is the nonlinearity for a SFWM process involving modes p, q, m, and n, given by:

$$\gamma_{pqmn} \propto \int \mathrm{d}x \int \mathrm{d}y f_p(x,y) f_q(x,y) f_m^*(x,y) f_n^*(x,y), \quad (3)$$

in terms of $f_m(x,y)$, the transverse field distribution for mode m. The single-photon spectrum, corresponding to frequency-resolved single-channel detection, is then:

$$S_s(\omega) \equiv \sum_\mu \langle \Psi | a_s^\dagger(\omega;\mu) a_s(\omega;\mu) | \Psi \rangle = \sum_m \sum_n \int \mathrm{d}\omega_i |G_{mn}(\omega,\omega_i)|^2. \quad (4)$$

Figure 1 shows our experimental setup. We employed a picosecond mode-locked Ti:sapphire laser (76 MHz repetition rate and 2 nm bandwidth centered at 692 nm, uncorrected for possible chirp) as a pump for the SFWM process. A prism-based bandpass filter (PBPF) with a slit configured to transmit the entire laser spectrum while blocking spurious photons at other frequencies filters the laser output. The filtered pump beam is coupled into a 12 cm length of bow-tie birefringent fiber (BRF; HB800G from Fibercore) using an aspheric lens with an 8 mm focal length; the polarization is adjusted with a half-wave plate (HWP1) so that the polarization becomes parallel to the slow axis of the fiber. The pump power, measured once out-coupled from BRF, is ~50 mW.

We used this fiber to generate photon pairs through cross-polarized SFWM, with the signal and idler photons polarized parallel to the fast axis of the fiber (orthogonally polarized to the pump). The figure inset shows a sketch of the fiber cross-section indicating the slow/fast axes as well the pump/SFWM polarizations. The photon pairs (along with remaining pump photons) are out-coupled from the fiber using a second aspheric lens with an 8 mm focal length. The polarization is once again adjusted with the help of a second half-wave plate (HWP2) so that the signal and idler photons become horizontally polarized. A Glan–Thompson polarizer (POL) reduces the remaining pump power by a factor equal to the extinction ratio of around 10^5. Note that POL suppresses any SFWM photon pairs resulting from processes with the same polarization for all four waves.

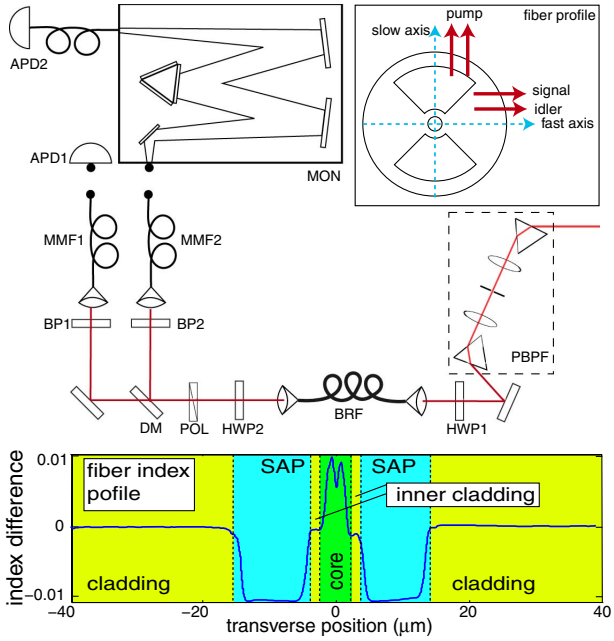

Fig. 1. Top: experimental setup; Bottom: fiber index profile.

The signal and idler photon pairs are frequency nondegenerate, emitted in spectral bands placed symmetrically around the pump. Thus, they may be split using a dichroic mirror (DM; >98% reflectivity within 350–676 nm and >93% transmissivity within 695–950 nm). In order to suppress any remaining pump photons, the low-wavelength arm is transmitted through a bandpass filter (BP1; >92% transmissivity within 584–676 nm and >5 optical densities suppression outside this range) while the high-wavelength arm is transmitted through a second bandpass filter (BP2; with >93% transmissivity within 768–849 nm and >5 optical densities suppression outside this range). Light in these two arms is coupled into multimode fibers (MMF1 and MMF2) using aspheric lenses with an 8 mm focal length. Each of the two arms may be detected directly, connecting the fiber in question to the input port of a fiber-coupled silicon avalanche photodiode (APD1) or may be detected with frequency resolution by transmitting the photons through a Czerny–Turner grating-based monochromator (MON) that has been fitted with a multimode fiber ouptut leading to a second silicon avalanche photodiode (APD2).

The first row in Fig. 2 shows frequency-resolved single-channel detection rates per 10 s for the low-wavelength, idler-mode [panel (a)] and for the high-wavelength, signal-mode [panel (b)] arms. Note that emission occurs in well-defined, energy-conserving signal and idler spectral peaks that are symmetric with respect to the pump frequency. We have identified four sets of peaks, labelled I through IV in panels (c) and (d). Note that in both arms there is a broadband background, probably due to spontaneous Raman emission.

The second row in Fig. 2 shows coincidence counts per 10 s in red, where each arm in turn is frequency-resolved [low-wavelength arm in panel (c) and high-wavelength arm in panel (d)] while photons in the remaining arm are detected directly. In each of the two panels we also have shown the accidental coincidence counts in green (obtained with a coincidence window configured so that the detected signal and idler photons correspond to two subsequent pump pulses). The third row in Fig. 2 shows the difference between measured coincidence counts and measured accidental coincidence counts [for the low-wavelength arm in panel (e) and for the high-wavelength arm in panel (f)].

Note that in the coincidence data (second row of Fig. 2), the broadband background attributed to spontaneous Raman scattering is essentially suppressed. In the data with accidental coincidences subtracted (third row of Fig. 2), the background is further suppressed resulting in four remarkably clean SFWM peaks. As we will show, these four peaks are related to distinct SFWM processes

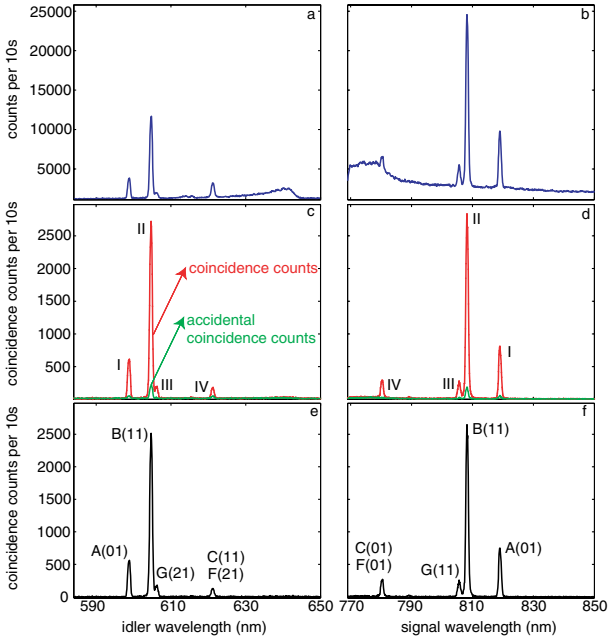

Fig. 2. Spectrally-resolved count rates for single-channel detection (1st row) and coincidence detection (2nd row). The accidentals-subtracted coincidence count rate is shown in the 3rd row.

for different phasematched combinations of transverse spatial modes for the pump, signal, and idler modes.

We have used as nonlinear medium a "bow-tie" fiber with a cross-section shown in the inset of Fig. 1, for which the GeO_2-doped SiO_2 core is surrounded by an inner SiO_2 cladding, and flanked by two low-index B_2O_3-doped SiO_2 stress-applying parts (SAPs) in the characteristic shape of bows. To obtain a theoretical description of the SFWM process, we first modeled the bow-tie fiber as a step-index fiber, determined by two parameters: the core radius r and the numerical aperture NA. We solve the characteristic equations to obtain the effective index of refraction $n^0_{lm}(\omega)$ for transverse mode LP_{lm}.

Second, we modeled the birefringence resulting from the SAPs by adding a constant offset Δ to the index refraction for light guided in the fiber and polarized along the x direction. Thus, we obtain $n_{lm,x}(\omega) = n^0_{lm}(\omega) + \Delta$ and $n_{lm,y}(\omega) = n^0_{lm}(\omega)$ for the x/y polarizations [14] (see Fig. 1 inset). For a given fiber, as specified by the three parameters $\{r, NA, \Delta\}$, we can then determine the wavenumber for the μ polarization (with $\mu = x, y$) and the LP_{lm} mode: $k_{lm,\mu}(\omega) = n_{lm,\mu}(\omega)\omega/c$. Note that the actual fiber is characterized by a complex, azimuthally asymmetric index of refraction gradient, so the fiber model used represents a considerable simplification.

For the specific values of the parameters $\{r, NA, \Delta\}$ that characterize our bow-tie fiber, the following transverse modes are supported at the operating frequencies: LP_{01}, LP_{11}, and LP_{21}. A given SFWM process involves a particular phase-matched combination of transverse modes for each of the four waves involved. Adopting the convention that the high-wavelength ($\lambda > \lambda_p$) peak corresponds to the signal photon and the low-wavelength ($\lambda < \lambda_p$) peak corresponds to the idler photon, we have identified seven distinct processes summarized in Table 1 that may occur (i.e., for which $\Delta k_{pqmn} \approx 0$ and for which γ_{pqmn} has appreciable values). Note that while in these processes the two pumps are frequency-degenerate, they can be nondegenerate in transverse mode.

For a theoretical description, our aim was to determine values for the parameters $\{r, NA, \Delta\}$, desirably close to those provided by the fiber manufacturer, which lead to simulation results that best fit the measured SFWM spectra in Figs. 2(e) and 2(f). We tested the possibility of each of the four matched peaks (I through IV) being explained by any of the seven processes in Table 1. We varied the birefringence within the range $4.0 < 10^4\Delta < 5.0$ and discarded any combinations of processes that do not lead to simultaneous phase matching at the frequencies of these four SFWM peaks within the parameter ranges $1.4\ \mu\text{m} < r < 2.5\ \mu\text{m}$ and $0.14 < NA < 0.3$.

Our specific procedure involved fixing the signal and idler frequencies to the maxima of peaks I through IV, and for each Δ value plotting contours $\Delta k_{pqmn} = 0$ (one for each pair of peaks) in $\{r, NA\}$ space, where a quadruple contour intersection indicates the desired solution. This leads, on the one hand, to the conclusion that only combinations of processes A, B, G, and C or A, B, G, and F can be responsible for peaks I, II, III, and IV, respectively. On the other hand, this also gives us a prediction for the values of the three parameters: $\Delta = 4.2 \pm 0.1 \times 10^{-4}$, $r = 1.6 \pm 0.1\ \mu\text{m}$, and $NA = 0.27 \pm 0.02$. It is interesting to note that the core diameter $2r$ obtained ($3.8\ \mu\text{m}$) is compatible with the mean field diameter provided by the manufacturer as $3.7\ \mu\text{m} < d_{\text{MFD}} < 4.9\ \mu\text{m}$; likewise, the birefringence Δ is compatible with the value provided, as $\Delta > 4.2 \times 10^{-4}$.

The numerical aperture obtained, however, is outside the range provided of $0.14 < NA < 0.18$. To understand this difference, we presented at the bottom of Fig. 1 the index difference (between the index of refraction and a reference value for SiO_2) profile along the bow-tie as measured by Fibercore Ltd., at a wavelength of 670 nm for the specific batch of fiber we used. The NA is given by $\sqrt{n_1^2 - n_2^2}$, where n_1/n_2 are the core/cladding indices of refraction; the value of NA provided was obtained by taking a representative value of the core index as n_1 (see bottom of Fig. 1), and the inner cladding index as n_2. Taking the SAP index as n_2 leads to a value of $NA \approx 0.24$, which is much closer to that obtained from our simulation-experiment comparison. This result suggests that the guided mode is in fact large enough to reach the inner portions of the SAPs. Note that Fibercore

Table 1. Allowed SFWM Processes, Involving the Pumps (p1 and p2), Signal(s), and Idler(i) Waves[a]

Process	p1	p2	$i(\lambda < \lambda_p)$	$s(\lambda > \lambda_p)$
A	01	01	01	01
B	11	11	11	11
C	01	11	11	01
D	01	11	01	11
E	21	21	21	21
F	01	21	21	01
G	11	21	21	11

[a]Two-digit numbers are the LP_{lm} mode labels.

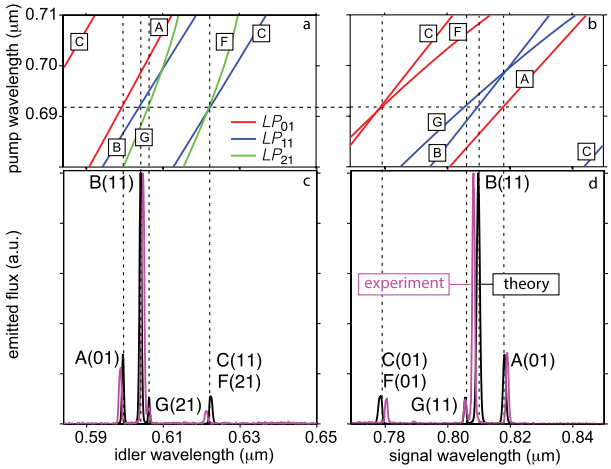

Fig. 3. Idler-pump and signal-pump phasematching diagrams for processes A-G (1st row). Comparison of experimental and simulated SFWM spectra (2nd row).

Ltd., has nonconclusive evidence that the guided mode can reach the inner portions of the SAPs.

In Figs. 3(a) and 3(b) we show phase-matching contours (defined by the condition $\Delta k_{pqmn} = 0$), assuming the fiber parameters found above for each of the combinations of processes A through G shown Table 1, as a function of pump and signal/idler wavelengths. For our pump wavelength ($\lambda_p = 692$ nm; note the horizontal dotted line), we may read out from panel (a) the idler ($\lambda < \lambda_p$) and from panel (b) the signal ($\lambda > \lambda_p$) generation wavelengths. Panels (c) and (d) show the experimental data in magenta (similar to panels (e) and (f) in Fig. 2), overlapped with our simulation results in black [based on Eq. (4)]. We have added to each peak [also in Figs. 2(e) and 2(f)] a label indicating with a capital letter the associated SFWM process (from Table 1) and with a two-digit number the associated *LP* mode. To compute the theory curves, we needed values for the pump power fraction W_{lm} coupled into mode LP_{lm} for the three modes involved. Three equations are obtained from: (i) the ratio of the heights of low-wavelength peaks I and II is proportional to $(W_{11}/W_{01})^2$; (ii) the ratio of the height of low-wavelength peaks II and III is proportional to W_{11}/W_{21}; and (iii) $W_{01} + W_{11} + W_{21} = 1$. While the heights of peaks I through III are used as inputs in this calculation, the height of peak IV can be predicted from the other heights, which leads to a useful self-consistency check.

Transverse-mode entanglement can occur for certain combinations of SFWM processes. For example, a hyper-entangled state with a Bell state embedded in transverse mode would result if processes C and D were phase matched at identical signal/idler frequencies.

In summary, we have demonstrated the generation of photon pairs in a birefringent bow-tie fiber by multiple SFWM processes resulting from different phase-matched combinations of transverse modes for the pump, signal, and idler waves. We associated the measured spectral peaks with distinct SFWM processes. Because the allowed combinations of modes are correlated to emission frequency, spectral filtering can be used to enable or disable specific processes and thus configure the resulting spatiotemporal entanglement for specific needs.

This work was supported by CONACYT, Mexico, by DGAPA (UNAM) and by AFOSR grant FA9550-13-1-0071.

References

1. J. P. Torres, K. Banaszek, and I. A. Walmsley, Prog. Opt. **56**, 227 (2011).
2. P. J. Mosley, A. Christ, A. Eckstein, and C. Silberhorn, Phys. Rev. Lett. **103**, 233901 (2009).
3. M. F. Saleh, B. E. A. Saleh, and M. C. Teich, Phys. Rev. A **79**, 053842 (2009).
4. M. Karpiński, C. Radzewicz, and K. Banaszek, Opt. Lett. **37**, 878 (2012).
5. Y. Kang, J. Ko, S. M. Lee, S.-K. Choi, B. Y. Kim, and H. S. Park, Phys. Rev. Lett. **109**, 020502 (2012).
6. R. H. Stolen and J. E. Bjorkholm, IEEE J. Quantum Electron. **18**, 1062 (1982).
7. L. E. Vicent, A. B. U'Ren, R. Rangarajan, C. I. Osorio, J. P. Torres, L. Zhang, and I. A. Walmsley, New J. Phys. **12**, 093027 (2010).
8. B. J. Smith, P. Mahou, O. Cohen, J. S. Lundeen, and I. A. Walmsley, Opt. Express **17**, 23589 (2009).
9. C. Soller, O. Cohen, B. J. Smith, I. A. Walmsley, and C. Silberhorn, Phys. Rev. A **83**, 031806(R) (2011).
10. B. Fang, O. Cohen, and V. O. Lorenz, J. Opt. Soc. Am. B **31**, 277 (2014).
11. Q. Zhou, W. Zhang, J. Cheng, Y. Huang, and J. Peng, Opt. Lett. **34**, 2706 (2009).
12. E. Meyer-Scott, V. Roy, J.-P. Bourgoin, B. L. Higgins, L. K. Shalm, and T. Jennewein, Opt. Express **21**, 6205 (2013).
13. K. Garay-Palmett, H. McGuiness, O. Cohen, J. Lundeen, R. Rangel-Rojo, A. B. U'Ren, M. Raymer, C. McKinstrie, S. Radic, and I. A. Walmsley, Opt. Express **15**, 14870 (2007).
14. J. Noda, K. Okamoto, and Y. Sasaki, J. Lightwave Technol. **4**, 1071 (1986).